Tracking the formation, fate and consequence for catalytic activity of Pt single sites on CeO_2

Florian Maurer[†], *Jelena Jelic*[#], *Junjun Wang*[‡], *Andreas Gänzler*[†], *Paolo Dolcet*[†], *Christof Wöll*[‡], *Yuemin Wang*[‡], *Felix Studt*[#], *Maria Casapu*[†], *Jan-Dierk Grunwaldt*[†*]

[†] Institute for Chemical Technology and Polymer Chemistry (ITCP), Karlsruhe Institute of Technology (KIT), Engesserstraße 20, 76131 Karlsruhe, Germany

[#] Institute of Catalysis Research and Technology (IKFT), Karlsruhe Institute of Technology (KIT), Hermann-von-Helmholtz-Platz 1, 76344 Eggenstein-Leopoldshafen, Germany

[‡] Institute for Functional Interfaces (IFG), Karlsruhe Institute of Technology (KIT), Hermann-von-Helmholtz-Platz 1, 76344 Eggenstein-Leopoldshafen, Germany

Corresponding author: *grunwaldt@kit.edu

KEYWORDS: single sites; ceria; platinum; operando X-ray absorption spectroscopy; density functional theory; infrared spectroscopy

Abstract and TOC

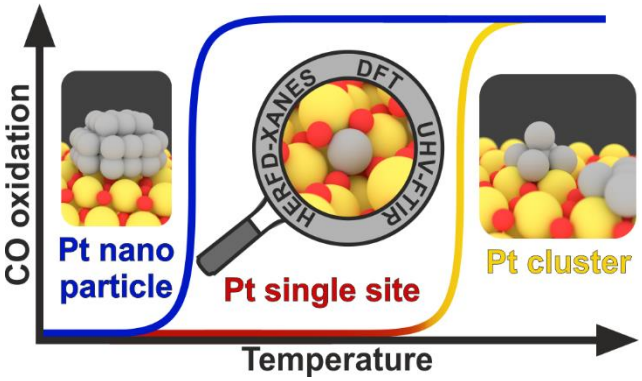

Pt single sites are highly attractive due to their high atom economy and can be generated on CeO_2 by an oxidative high-temperature treatment. However, their location and activity are strongly debated. Furthermore, reaction-driven structural dynamics have not been addressed so far. Here, we were able to evidence Pt-induced CeO_2 surface restructuring, locate Pt single sites on CeO_2 and track the variation of the active state under reaction conditions using a complementary approach of density functional theory calculations, *in situ* infrared spectroscopy, *operando* high-energy-resolution fluorescence detected X-ray absorption spectroscopy and catalytic CO (as well as C_3H_6 and CH_4) oxidation. We find that the onset of CO oxidation is linked to the migration of Pt single sites from four-fold hollow sites to form small clusters containing few Pt atoms. This demonstrates that *operando* studies on single sites are essential to assess their fate and the resulting catalytic properties.

INTRODUCTION

Precious metals are extensively used as heterogeneous catalysts, with emission control being one of the most important applications.[1] The costs and scarcity associated with the use of noble metals motivates the search for solutions with substantially reduced noble metal contents.[2–4] Single atom catalysts (SAC) hold such

a promise as they lower the noble metal content significantly as all atoms are potentially active species.[5–9] Exploiting the strong noble metal support interaction between Pt and CeO_2, metallic Pt particles can be formed or – in contrast to weakly interacting supports like Al_2O_3 – redispersed, with tremendous impact on the catalyst activity.[10–13] The preparation of SAC has been demonstrated for Pt, which can be atomically dispersed when using CeO_2 as a support through an oxidizing treatment at 800 °C.[14]

However, the exact structure of the single sites, their reactivity and, particularly, their state and dynamics during reaction are still unknown and heavily debated.[4,15,16] The location of Pt single sites is claimed to range from surface adsorbates on {111} ceria steps,[17,18] {111},[19] {110}[20,21] or {100}[6,22,23] ceria facets to surface[21,24,25] or bulk Ce substitutes[26–28] forming $Ce_{1-X}Pt^{2+}_XO_{2-Y}$-composites. During change of the gas atmosphere and of the temperature, the structure of the single sites may strongly change resulting in a new and more active state. For example, after a high temperature treatment strong Pt-O-Ce bonds are reported to over-stabilize the single sites which are thus less active.[29] During the catalytic oxidation, oxygen is suggested to be provided by the support, while the reactant e.g. CO is adsorbed directly on Pt,[22,25] similar to Pt nanoparticles on CeO_2.[30] Bera *et al.* correlated the intensity of the Pt-O-Ce bond observed by Extended X-ray Absorption Fine Structure (EXAFS) measurements with the catalytic activity for $Ce_{1-X}Pt^{2+}_XO_{2-Y}$,[31] and Nie *et al.*[24] demonstrated that the catalytic activation of a Pt single atom catalyst can be increased by steam treatment. It is suggested that this treatment leads to the formation of $Ce_{1-X}Pt^{2+}_XO_{2-Y}$H-OH species that are catalytically more active than $Ce_{1-X}Pt^{2+}_XO_{2-Y}$.[24] In contrast, other studies report an increase in catalytic activity after a reductive treatment at temperatures below 300 °C.[9,32–34] Importantly, such

reductive treatment has been shown to induce segregation of highly dispersed Pt generating small nanoparticles (< 2 nm) that are very active for CO- and C_3H_6 oxidation.[35]

Despite of all these efforts, an in depth understanding of the influence of reaction conditions on the stability of Pt single sites is still missing. This directly relates to the assignment of the catalytic activity to specific active sites and whether these are really the Pt single sites. Addressing this requires elaborate and systematic *operando* studies. Particularly, combining complementary spectroscopic techniques and DFT-calculations represents a powerful approach,[36,37] which was exploited in the present study.

Herein, we present a comprehensive investigation on the nature of atomically dispersed platinum supported on CeO_2, the dynamic changes enforced during oxidation reactions and the impact on the assessment of the activity of such catalytic systems. We use the complementary application of *operando* high-energy-resolution fluorescence detected X-ray absorption spectroscopy (HERFD-XAS), *in situ* infrared spectroscopy (IR), and density functional theory calculations (DFT) to track the formation, fate and activity of Pt species during CO, C_3H_6 and CH_4 oxidation.

RESULTS

Pt single sites and nanoparticles catalysts. A Pt/CeO_2 catalyst with a low surface area of 28 m^2/g, to prevent sintering and gain a stable support, was hydrothermally treated (10% H_2O, 10% O_2, 800 °C, 16 h) to generate Pt single sites (Pt-SS).[14] Despite its low surface area (25 m^2/g after hydrothermal aging), the low Pt loading (0.94 wt.%) is significantly below a monolayer (ML; see Supplementary Fig. 14). A reference catalyst containing Pt nanoparticles (Pt-NP) was prepared by reduction of Pt-SS at 400 °C (2% H_2 for 30 min).[35,38] No Pt reflections were found for both samples in the corresponding XRD patterns, indicating the presence of very small Pt entities (Supplementary Fig. 1). TEM results (Fig. 1a and b) confirmed the presence of small, homogenously distributed Pt nanoparticles of ~1 nm for the Pt-NP sample, while no Pt particles were identified for the Pt-SS catalyst. According to the X-ray photoelectron spectroscopy (XPS) measurements (Fig. 1c and d), the Pt oxidation state is about 0 for Pt-NP (characterized by the Pt 4f doublet at 71.4/74.7 eV). In agreement with previous theoretical and experimental studies on Pt single sites on CeO_2, a predominant +2 oxidation state (72.9/76.2 eV) was found for the Pt-SS,[14,22,25,39] while the amount of Pt^{4+} species (74.3/77.6 eV) was only minor. Based on surface quantitative analysis, the atomic ratios between Pt and Ce was estimated to be 2.5:97.5 for Pt-SS (Pt single sites) and 2.0:98.0 for Pt-NP (Pt nanoparticles). Considering that both catalysts contain the same amount of Pt and Ce, the higher Pt/Ce atomic ratio of Pt-SS (by about 25%) reveals the presence of highly dispersed Pt species, in line with the TEM observations. The corresponding Ce3d core-level spectra for both catalysts are shown in Supplementary Fig. 12. For Pt-NP, the content of Ce^{3+} species (formed along with the reduction of Pt-SS, due to UHV-conditions) was estimated to be 35 %.

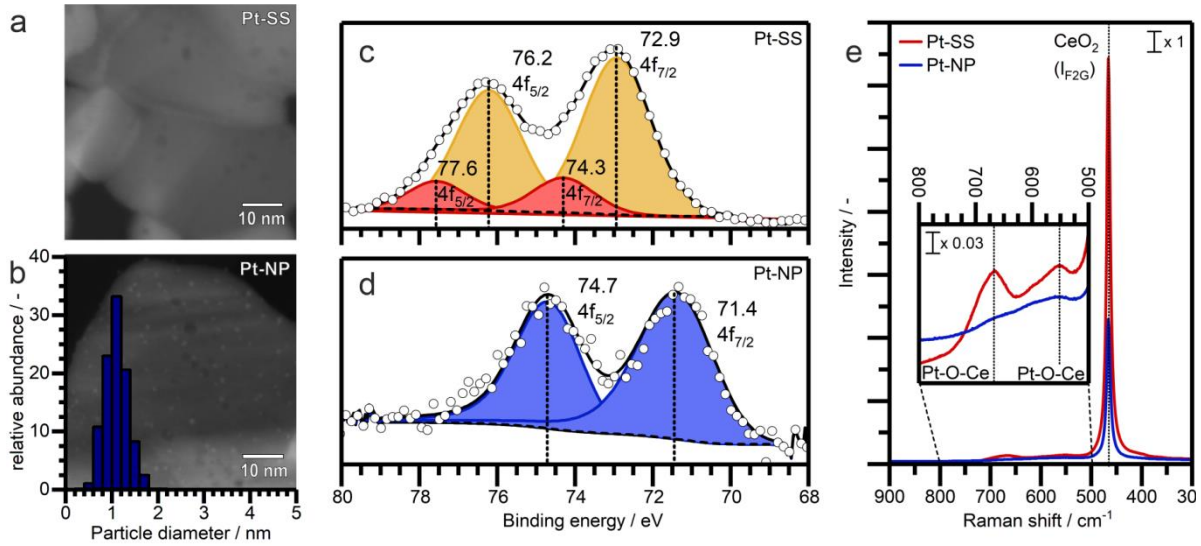

Fig. 1: ***Ex situ*** **characterization of Pt-SS and Pt-NP.** HAADF-STEM images of Pt-SS (a) and Pt-NP including a particle size distribution (b). No Pt-particles were found for the Pt-SS catalyst, while mono disperse particles around 1 nm where found for Pt-NP. XPS results show Pt to be in oxidation state +2 in orange and partially +4 in red colour in case for the Pt-SS (c) and 0 (blue) for Pt-NP (d). In contrast to Pt-NP, pronounced bands at 552 cm^{-1} and 667 cm^{-1} were found in the Raman spectra for Pt-SS (e). These features are characteristic for Pt/CeO_2 materials typically assigned to Pt-O or Pt-O-Ce and indicate a highly oxidized state of Pt-SS.

Raman spectroscopic characterization (Fig.1e) underlines these findings, showing distinct features at 552 cm^{-1} and 667 cm^{-1} typical for the Pt-SS. These bands have been previously assigned to vibrations originating from Pt-O or Pt-O-Ce bonds.[29,40] In contrast, these features were not found for the reduced Pt-NP sample.

Locating Pt single sites on CeO_2. At first, we investigated the stability of Pt^{2+} (formal charge, cf. Fig. 1c and d) single atoms on the ceria support by means of DFT calculations for various locations and binding geometries. Hereby, we considered Pt adsorbed on the surface as well as Pt substituting a cerium atom on the surface and in the bulk. CeO_2{111}, CeO_2{110}, Ce{100} as well as CeO_2{211} and CeO_2{221} were taken for the surface adsorption and substitution of Pt. The latter represent intersections between different facets and have local {100} and {110} geometries, respectively (for detailed structures, see Supplementary Figs. 15-19).

We found that the stability of adsorbed Pt^{2+} relative to PtO_2 (g) at 800 °C increases from CeO_2{111} (+2.16 eV) to CeO_2{110} (+1.41 eV) and is the strongest for CeO_2{100} (+0.9 eV). Hence, the adsorption energy of Pt^{2+} increases with an increase of the coordination number of Pt adsorbed on the surface. Note, that a single Pt^{2+} atom being adsorbed on CeO_2{100} at low coverage exhibits empty neighbouring four-fold hollow sites resulting in an imperfect square planar geometry (cf. inset in Fig. 2), where Pt^{2+} is surrounded by only 3 oxygen atoms (cf. Supplementary Fig. 17c). This can be overcome either by rearranging the surface oxygen atoms, as Ce^{4+} is less sensitive to oxygen coordination (Pt^{2+} adsorption energy of +0.23 eV for a coverage of 0.25 ML), or by increasing the coverage of Pt^{2+} to 0.5 or 1 ML, which achieves +0.12 eV adsorption energy (for detailed structures see Supplementary Fig. 17). The strong adsorption of Pt^{2+} within the geometry of the four-fold hollow site is observed at the {211} edge, which also exhibits {100} like facets. In this case, we calculated the Pt^{2+} adsorption to be 0.34 eV at low coverage and 0.19 eV at a coverage of 1ML (see Supplementary Fig. 18). Substitution of Pt^{2+} into the ceria surface is calculated to be less stable (2.05 eV, 0.67 eV and 0.66 eV for {111}, {110} and {221}, respectively) as is Pt^{4+} substitution into the bulk (2.28 eV). Other adsorption geometries for Pt^{4+} as well as for Pt^0 have also been investigated and are found, except at low coverage for {100}, to be less stable (all values are given in Supplementary Table 5 and 6, as well as the corresponding phase diagrams, Supplementary Figs. 21-25). For Pt^0, the Bader charge analysis (cf. Supplementary Table 11 and 12) showed to some extent an oxidation of Pt and a corresponding reduction of Ce in most cases. For simplicity, these structures are referred to as Pt^0.

While the adsorption at 4 fold hollow sites is most favourable, the surface energy of facets showing this geometry is much higher (11.1 eV/nm^2 for {100}) compared to the close-packed {111} and {110} facets with 4.6 and 7.7 eV/nm^2, respectively.[41] We therefore speculate that the ceria support is initially primarily comprised of {111} and {110} facets (including CeO_2{221} intersection between them) and that the presence of Pt^{2+} atoms induces restructuring of the ceria surface creating 4-fold hollow sites as it can be found on the {100} surface, where platinum adsorbs and is stabilized. This would explain why these stable Pt-SS are formed during thermal treatment at 800 °C but not at 500 °C (Fig. 2), since the restructuring of the ceria support is kinetically hindered at low temperatures.[18,35]

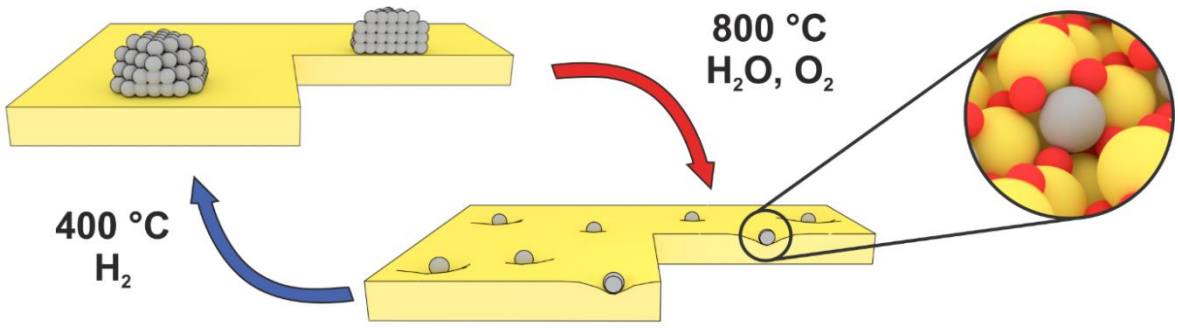

Fig. 2: Concept of the Pt-CeO_2 interaction. Illustration of Pt (●) nanoparticle redispersion and Pt induced restructuring of the CeO_2 (inset: ● Pt, ● Ce, ● O) support at high temperatures as well as particle formation from the atomically dispersed state under reducing conditions.

In order to confirm the chemical and structural surroundings of Pt single sites as determined by DFT modelling, the basic facets {111}, {110}, {100} (Fig. 3g-k), and the edges {221} and {211} were used to fit experimental Extended X-ray Absorption Fine Structure (EXAFS) spectroscopy data (Fig. 3a-e, Supplementary Fig. 2 and Supplementary Table 1). Structures featuring shorter Pt-O bonds and additional oxygen (Pt^{4+}-like structures; cf. Supplementary Fig. 2 and Supplementary Table 2) were less suited to fit the EXAFS data. In agreement with the Gibbs free energy of Pt^{2+} adsorption on the {111} facet, a model based on this structure is not able to fit

the EXAFS spectrum (Fig. 3a). Especially, the first O coordination sphere at 1.59 Å is poorly represented by this configuration and the analogous structure on {110} ceria (Fig. 3c). While Pt^{2+} located in the four-fold hollow sites of the {100} facet is able to render this feature, shells above 2.25 Å are not reproduced correctly (Fig. 3e). In contrast, the theoretically calculated EXAFS data for Pt^{2+} adsorbed at the {211} edge (created during surface reconstruction) mimics very well the experimental one (cf. Supplementary Fig. 2d; misfit factor of 3.3 %).

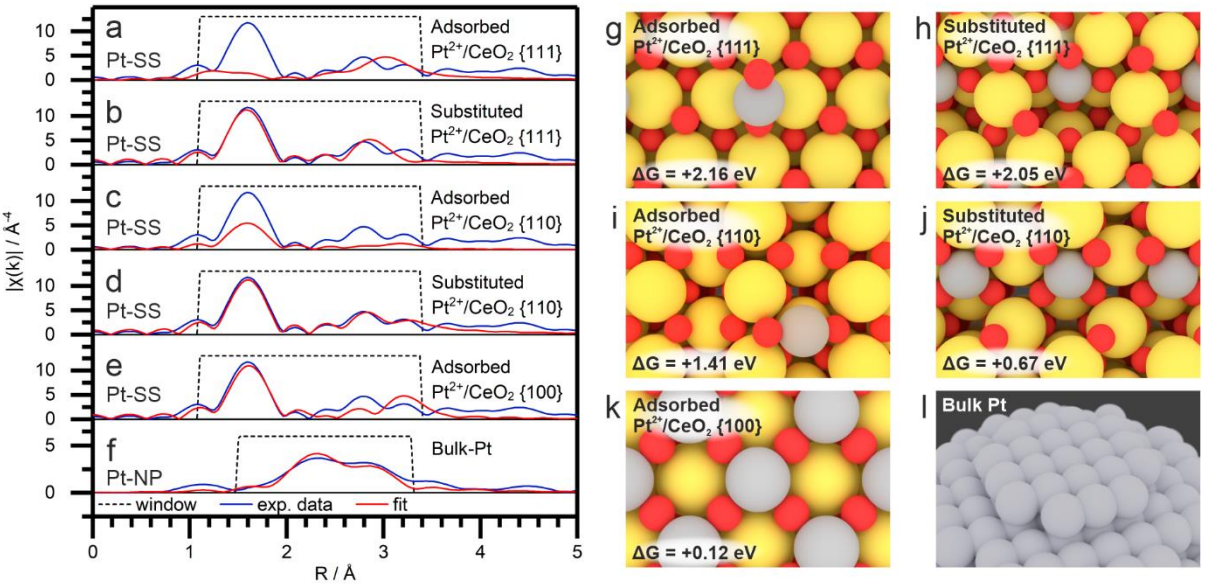

Fig. 3: EXAFS analysis of the Pt-SS catalyst. Fourier transformed (FT) k^3-weighed EXAFS data of Pt-SS (a-e) and Pt-NP (f) recorded at the Pt L_3-edge (k-range: 3-12 Å). Experimental data (blue) were fit (red) using five possible locations for the Pt^{2+} (●) ranging from an adsorbed species on {111} (a), {110} (c) or {100} (e) CeO_2 (● Pt, ● Ce, ● O) facet to substituted species in the {111} (b) and {110} (d) facets. Bulk Pt was used to fit Pt nanoparticles (f). The corresponding structures are depicted in g-l.

Going from adsorbed to surface substituted Pt species, the fit improves significantly for several exposed facets. Models with Pt^{2+} substituted on the {110} lattice (Fig. 3d, Supplementary Fig. 3 and Supplementary Table 3) can reproduce all features within the fitting range (1.1-3.4 Å; misfit factor of 2.2 %). In line with our DFT calculations, the preferential location of Pt^{2+} ions on the {110} ceria surface has been also previously reported for isolated ions and for small PtO_X clusters.[20,21] Hence, by

benchmarking all relevant Pt adsorption and substitution sites from our DFT models against the experimental findings, a direct spectroscopic assignment is provided: Under oxidizing conditions at elevated temperatures Pt single sites are solely formed at four-fold hollow sites on CeO_2, i.e. as Pt^{2+} substitute {110} or Pt^{2+} adsorbate on {211}, with perfect square planar geometry involving Pt-O-Ce bonds.

For the Pt-NP reference catalyst, EXAFS analysis (Fig. 3f) indicates an average Pt particle diameter of 0.9-1.0 nm, confirming the findings from TEM characterization (~1.1 nm; cf. Supplementary Fig. 5 and 6 and Supplementary Table 4).

Interaction of Pt single sites with gas adsorbates. Despite the identification of the Pt location in ceria-supported single site catalysts being important, the interplay with the components of the reaction gas mixture is a more relevant indicator for the catalytic behaviour and structural variations. Moreover, the interaction with gas molecules gives the opportunity to probe the presence of Pt on the ceria surface. Hence, complementary UHV-FTIRS, DRIFTS and *in situ* HERFD-XAS measurements were performed as a next step.

Using CO as probe molecule, the outermost layer of the catalyst material can be selectively characterized by UHV-FTIRS and conventional DRIFTS. Note that conventional DRIFTS at 298 K in CO may be critical as it can change the sample but serves as a good reference point to other studies that report a band at 2090 cm^{-1} to be an indicator of Pt-SS.[14,42] Thus the Pt-SS catalyst was exposed at first in a UHV-FTIRS to 0.01 mbar CO at a low temperature of 113 K. Three features at 2179 cm^{-1}, 2161 cm^{-1} (Fig. 4a, red) and 2129 cm^{-1} appear. Previous results indicate that the IR-band at about 2170 cm^{-1} can be attributed to the CO adsorption at Ce^{3+} defect sites.[43] This assignment could be confirmed also in the present study, with pure ceria showing one distinct feature at 2168 cm^{-1} (Fig. 4d, e and Supplementary Fig. 7). For

the Pt-SS catalyst, the band corresponding to CO adsorption on pure CeO_2 is slightly shifted towards lower wavenumbers (2161 cm^{-1}). This could be due to the rather high extent of Pt substitution/adsorption affecting the chemical environment of nearly 50 % of the CeO_2 surface and thus the adsorption sites, even if Pt is not the next nearest neighbour (cf. Supplementary Fig. 13 and 14). It could also be caused by the slight restructuring of the CeO_2 surface induced during Pt single site formation. Since direct CO-adsorption on oxidized Pt species results in CO vibrations located between 2090 and 2140 cm^{-1},[42] the feature at 2129 cm^{-1} was assigned to CO physisorption on oxidized Pt^{2+} species by DFT calculations (Fig. 4f and Supplementary Table 8). The largely blue-shifted feature at 2179 cm^{-1} can be only attributed to CO adsorbed on surface Ce ions in the direct vicinity of Pt. Given that the approach using IR and CO adsorption is extremely sensitive to the outermost surface of catalysts, the observation of the predominant peak at 2179 cm^{-1} indicates that Pt-substitution occurs at the ceria surface. DFT calculations of the vibrational frequencies for Pt single sites and different pure ceria facets confirm these assignments and especially the blue shift due to Pt-substitution (cf. Supplementary Table 8). Overall, there is a good agreement between computed and experimental frequencies (Fig. 4). The intensity difference of the CO bands observed in Fig. 4a could be explained in terms of the different transition dipole moments (TDM) of the vibrations[44] as well as the low surface concentration of highly dispersed Pt single atoms.

For the same Pt-SS sample, predominant adsorption of CO on Pt was observed at higher temperatures (298 K) and CO partial pressure (20 mbar), which resulted in a distinctive band at 2090 cm^{-1} (Fig. 4b). This feature has been earlier reported for single site Pt species and, thus, our catalyst is analogous to those reported in

literature.[14,42] According to our DFT calculations, however, a slight distortion of Pt^{2+} (by 0.8 Å) is observed upon CO chemisorption (see Supplementary Fig. 26). As illustrated in Fig. 4g, Pt is relocated out of the four-fold hollow sites of CeO_2. This evolution of the single site is further supported by the UHV-FTIRS data obtained for a Pt/CeO_2 sample thermally treated at milder conditions (10 % O_2 at 600 °C; Fig. 4a, black). As we previously reported, at such lower temperatures an oxidative treatment leads to highly dispersed and oxidized Pt species on the surface of CeO_2.[45] In line with the prediction of the DFT calculations and EXAFS analysis, the absence of the IR band around 2090 cm^{-1} for Pt-SS under UHV conditions is a direct evidence for a Pt-induced restructuring of the CeO_2 surface creating additional four fold hollow sites for Pt^{2+} adsorption at 800 °C. Furthermore, the appearance of a feature at 2090 cm^{-1} at higher CO partial pressure and temperatures clearly shows the change of the single site local structure already at room temperature, which is once again in agreement with our DFT calculations. Note that due to the lower binding energy of CO on CeO_2, only a weak feature at 2167 cm^{-1} was found in DRIFTS (Fig. 4b). Additionally, some CO physisorbed on remaining Pt^{2+} species led to the appearance of the IR band at 2121 cm^{-1}.

Complementary to IR spectroscopy we applied HERFD-XANES spectroscopy, as it allows element specific detection of changes in the local structure, coordination and interaction with different ligands due to its high energy resolution[46,47] and showed already promising results for other classes of single atom catalysts.[48] After an oxidative treatment in 10% O_2 at 500 °C followed by a subsequent cooling, Pt-SS exhibits a distinct white line feature at 11,567.6 eV (Fig. 4c and Supplementary Fig. 10f). Its intensity significantly decreases during a dropout of oxygen and exposure to an inert gas atmosphere. Sofanova *et al.* found a similar pronounced response of the

white line intensity for a Pt/Al_2O_3 catalyst containing Pt-nanoparticles.[46] In their study, the interaction with oxygen led to an increased white line due to the partial oxidation of the pre-reduced Pt-species. According to the XPS and EXAFS analysis, the oxidation state of Pt was found to be +2 for the Pt-SS sample. Therefore, the decrease of the white line during the change from an oxidizing to an inert atmosphere is traced back to the desorption of adsorbed oxygen. This assumption is supported by FDMNES calculations (cf. details in the Supplementary discussion) of Pt^{4+}/{110}-CeO_2 and Pt^{2+}-O_2/{110}-CeO_2 with interfacial oxygen between the noble metal and CeO_2 (cf. Fig. 6 and Supplementary Fig. 29). In comparison to the Pt state in an inert atmosphere, the switch to 1000 ppm CO/He causes a minor shift of the

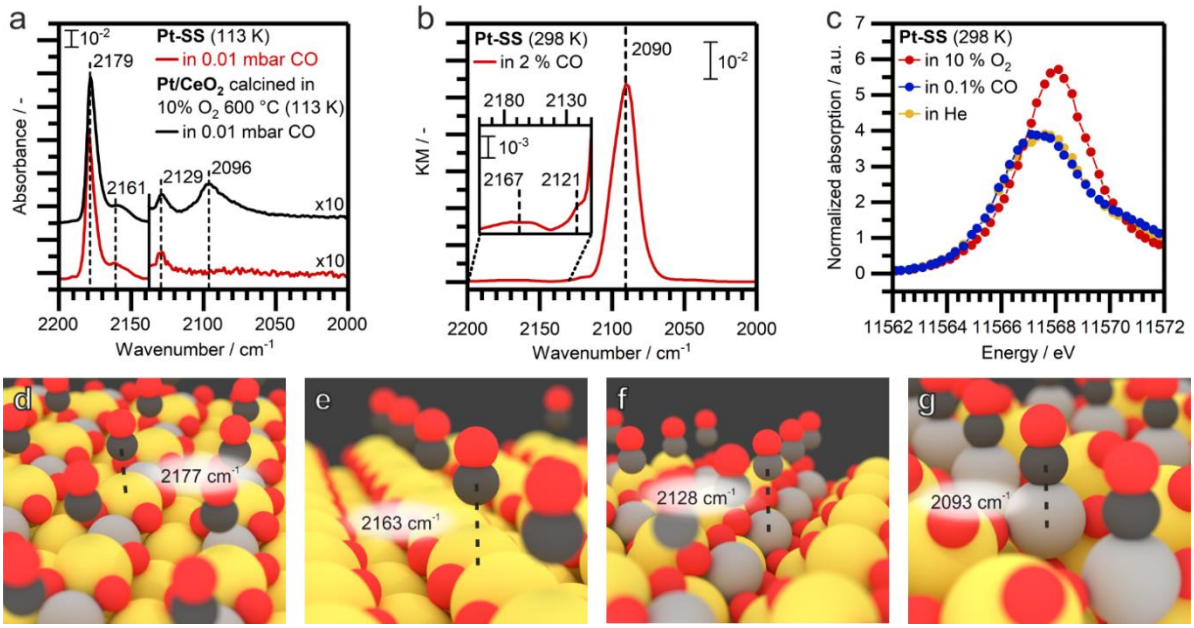

Fig. 4: Interaction of Pt-SS with gas phase adsorbates. UHV-FTIRS in 0.01 mbar CO at 113 K (a) of Pt-SS (red) and of a thermally treated (10% O_2, 600 °C) Pt/CeO_2 catalyst (black), DRIFTS in 2% CO at 298 K (b) and HERFD-XAS (after oxidative pre-treatment at 500 °C) in 10% O_2, pure He or 0.1% CO at 298 K (c) of the as prepared Pt-SS. Corresponding structures and CO vibrational frequencies of the DFT calculations (d-g; ● Pt, ● Ce, ● O, ● C). UHV-FTIRS of Pt-SS proves the substitution of Pt into the CeO_2 lattice. HERFD-XAS spectra towards changes in the gas phase confirm the location of Pt-SS in the utmost layer of CeO_2.

white line towards lower adsorption energies by 0.5 eV. This is in contrast to the reported behaviour of Pt-nanoparticles on Al_2O_3, where the white line is more pronouncedly shifted towards higher energies due to the adsorption of CO bridging two Pt atoms.[46]

We thus conclude that the distinct variation of the near edge region upon changes in reaction mixture demonstrates two characteristics of Pt single site species: The majority of Pt sites is located on the surface of CeO_2 and adsorption/desorption of gas phase species occurs even at room temperature. This is supported by our IR results (Fig. 4a) and in line with reports using surface sensitive characterization techniques like low energy ion scattering (LEIS) or XPS, as well as theoretical calculations.[18,21] Hence, both, the Pt-SS and Pt-NP catalyst, provide Pt on the surface and are ideal for comparison in catalytic tests.

Oxidation activity of Pt single sites. The CO, C_3H_6 and CH_4 oxidation activity of Pt-SS under oxygen rich conditions was thus compared to that of Pt-NP (Fig. 5). In all three cases, Pt-NP showed a higher catalytic activity than Pt-SS, with the difference in T_{50} (temperature of 50% conversion) being 125 °C and 66 °C for CO and C_3H_6 oxidation, respectively. The high activity of such Pt-NP is well known in literature.[35] In case of CH_4 oxidation, Pt-SS reached a maximum of 10 % conversion at 500 °C, which is in a similar order of magnitude as that obtained for the Pt single site catalyst supported on Fe_2O_3.[49] In contrast, the same conversion was measured below 300 °C for Pt-NP and over 90% CH_4 oxidation was achieved at 420 °C for the same catalyst. The beneficial effect of a pre-reduction step was also found on Pd-based CH_4-oxidation catalysts.[50,51] However, above 460 °C, the catalytic

performance decreases again, which may be due to *in situ* reoxidation or even redispersion of Pt in lean reaction mixtures in an excess of oxygen.[35]

The catalytic activity for CO, C_3H_6 and CH_4 oxidation data indicates that despite of the maximum noble metal dispersion in the Pt-SS sample, this catalyst is outperformed by the Pt-NP during heating in the reaction mixture. As in Pt-NP the number of surface sites is lower than in Pt-SS, the TOF is even higher for Pt-NP. However, during cooling, Pt-NP (T_{50}=171 °C) and Pt-SS (T_{50}=175 °C) exhibit a very similar CO oxidation activity. Small Pt nanoparticles deactivate due to their oxidation and redispersion above 400 °C.[35] A normal hysteresis as found for Pt-SS is usually observed for larger Pt particles.[52] These variations in catalytic activity can originate from heat effects or structural changes during the transient measurements.[53] Such phenomena were found to be less pronounced for C_3H_6 or CH_4 oxidation (Fig. 5b and c). Hence, the possible structural variations of the single sites in Pt-SS were followed by *operando* (HERFD-) XAS investigations during CO conversion.

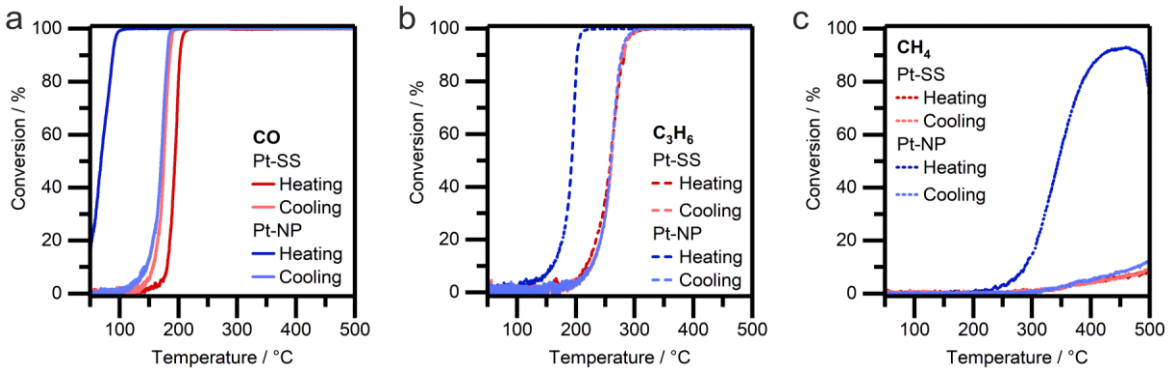

Fig. 5: Oxidation activity of Pt-SS and Pt-NP. Light-off curves during heating (10 K/min; dark colours) and cooling (light colours) of Pt-SS (red) and Pt-NP (blue) in a lean reaction mixture (8% O_2 in N_2) containing 1000 ppm CO (a), 1000 ppm C_3H_6 (b) and 1000 ppm CH_4 (c). Pt-NP is superior to Pt-SS in terms of oxidation performance.

***Operando* tracking of Pt single sites.** The CO-conversion during operando XAS and the oxidation state in terms of reduced Pt^0 (for spectra cf. Supplementary Fig. 11) are shown in Fig. 6a. In line with the laboratory tests, high CO conversion was

reached for Pt-NP below 100 °C and only above 200 °C for Pt-SS during the *operando* conventional XAS experiments. Pt-NP kept its initial oxidation state (77-79% reduced Pt) until full CO conversion was reached and is strongly oxidized at higher temperatures. In contrast, the as prepared Pt-SS catalyst was already highly oxidized in its initial state. Up to 150 °C no structural changes occurred for this sample, with little to no CO conversion. Only when Pt was reduced to a considerable extent (fraction of 38 % Pt^0 at 220 °C), CO conversion set in (Fig. 6a). The structural changes during the *operando* tests seem to be reversible: EXAFS analysis of Pt-SS before and after the catalytic tests confirmed the same single site structure for both catalyst states (cf. Supplementary Fig. 8). Consecutive light-off tests to 500 °C showed Pt-SS to be rather stable as well (cf. Supplementary Fig. 9). The structural changes occurring during start of CO-oxidation in the Pt-SS catalyst are difficult to derive from conventional XAS. Therefore, HERFD-XANES was additionally employed on Pt-SS to separate the plain reduction of single sites from restructuring processes.

HERFD-XANES spectra collected for the Pt-SS catalysts in reaction mixture (Fig. 6b; 1000 ppm CO, 10% O_2 in He), in a temperature range from 50-400 °C, show pronounced changes in the white line position and intensity. First, a steep decrease in intensity up to 150 °C is observed followed by a shift of the white line towards lower adsorption energies. In order to interpret intermediate structural states in the spectroscopic data, a linear combination analysis was performed using references obtained by a Multivariate Curve Resolution-Alternating Least Squares algorithm (MCR-ALS; cf. Supplementary Fig. 10)[54,55], which has been demonstrated as a highly efficient analysis method.[56] Four reference states corresponding to Pt^{4+}, Pt^{2+}, more reduced $Pt^{\delta+}$-CO as well as a Pt-cluster like $Pt_x^{\delta+}$-CO were extracted including

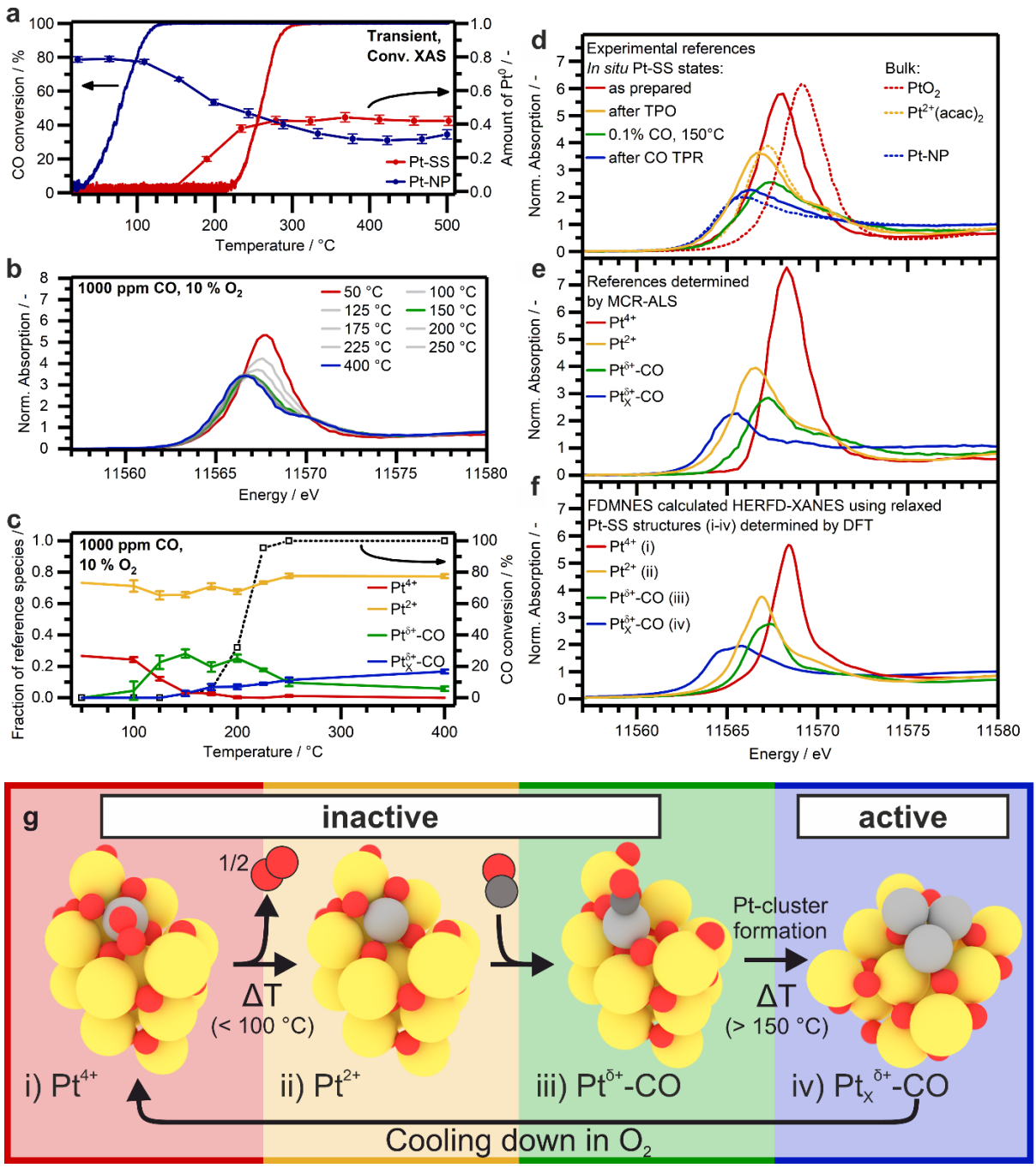

Fig. 6: Spectroscopic assignment of the active state. CO-conversion and results (with standard error) of the linear combination fitting of transiently recorded XANES spectra for Pt-SS and Pt-NP during heating (5 K/min) in 1000 ppm CO and 10% O_2 (a). *Operando* HERFD-XANES spectra of Pt-SS at different temperatures in reaction mixture (b; 1000 ppm CO, 10% O_2) under steady state conditions using a WHSV of 34,000 L/g_{Pt}/h. Catalytic activity during the HERFD-XANES experiments and fraction of Pt^{4+}, Pt^{2+}, $Pt^{\delta+}$ with adsorbed CO and $Pt_X^{\delta+}$ cluster, obtained by LCA (c; with standard error) using references obtained by MCR-ALS, experimental references (d), MCR-ALS derived references (e); and FDMNES calculated HERFD-XANES (f) using relaxed Pt-SS structures on the {110} facet (indexed i-iii) and on the {111} facet (indexed iv) determined by DFT and depicted in g). Proposed scheme of the reversible formation of catalytically active $Pt_X^{\delta+}$ cluster based on the *operando* HERFD-XANES results (g; ● Pt, ● Ce, ● O, ● C).

their quantitative distribution during heating in reaction mixture. The spectra of the corresponding species were systematically assigned based on *in situ* HERFD-XANES experiments (Fig. 6d and cf. Supplementary Fig. 10a and b) of Pt-SS under oxidizing (10% O_2/He) and reducing conditions (1000 ppm CO/He), bulk references, XPS data (Fig. 1; assignment of Pt^{2+} and Pt^{4+}), *in situ* UHV-FTIRS studies (Fig. 4; assignment of Pt^{2+}-CO), FEFF and FDMNES calculations (Figs. 6 and Supplementary Fig. 29) of the XANES spectra using the respective structures calculated by DFT (Fig. 6g).

Considering the poor thermodynamic stability of Pt^{4+} species (Fig. 6g-i) on the ceria surface irrespective of the exposed facet, the adsorption of oxygen occurs only in the low temperature range on the highly stabilized Pt^{2+} (Fig. 6g-ii) planar square hollow sites at the {110} facet, {221} or {211} edges. Accordingly, Pt seems to reduce during heating in 10% O_2 as illustrated by the *in situ* HERFD-XANES results (cf. Supplementary Fig. 10a). Complementary DFT calculations indicate that two types of interfacial oxygen exist. The first type corresponds to adsorbed oxygen, which is easily desorbed already at room temperature in an inert or CO containing atmosphere. Consequently, it is not expected to participate in the oxidation reaction. We identified two concurring structures that are very similar in energy but differ in their local geometry and oxidation state of Pt (more details, cf. Supplementary Fig. 27). A similar behaviour for Pt^{4+} at a {211} edge was claimed by Kunwar *et al.* involving molecular oxygen.[18] The second interfacial oxygen type appears due to the localization of Pt^{2+} at the four-fold hollow sites forming Pt-O-Ce bonds. Removing it from the system and thus reducing Pt, which is known as a necessary step for the CO oxidation onset, is rather difficult due to strong binding energies (cf. Supplementary Tables 9 and 10).

In contrast, regardless of their location on CeO_2, the adsorption of CO onto Pt^{2+} single sites is spontaneous with the {100} facet being most and {110} least favoured (cf. Supplementary Table 9). Reducing conditions (cf. Supplementary Fig. 10b and e, 1000 ppm CO/He) lead to complete oxygen desorption at 50 °C and Pt^{2+} is mainly covered with CO at 100 °C (Fig. 4g and Fig. 6g-iii). Above 100 °C, Pt^{2+} starts to reduce to $Pt^{\delta+}$-CO. The corresponding shift of the white line between 100-150 °C towards higher absorption energies can be found as well during formation of Pt^0 nanoparticles on Al_2O_3 due to the adsorption of CO.[46] Above 150 °C, the white line shifts towards lower energies indicating the formation of small $Pt_X^{\delta+}$ clusters (Fig. 6g-iv).

Hence, under reaction conditions (Fig. 6c and g), oxygen is desorbed from Pt^{4+} sites (Fig. 6g-i) below 100 °C. Up to 150 °C, over 22% of the Pt species underwent restructuring to $Pt^{\delta+}$-CO sites (Fig. 6g-iii). Nevertheless, the catalyst remained inactive in this state. This behaviour indicates that interfacial oxygen from CeO_2 is not available for this reaction under such conditions (single site state, low temperature), in line with our DFT calculations and recent studies.[20,24,29] Our results now reveal that such Pt-O-Ce bonds can be broken at temperatures above 150 °C in the reaction atmosphere applied here, leading to small $Pt_X^{\delta+}$ entities (Fig. 6g-iv). A similar CO assisted sintering in case of reducible supports was only proposed for a Pd/Fe_3O_4 catalyst under model conditions by Parkinson *et al.* using scanning tunnelling microscopy[57]. Once the formation of these clusters (approximately 2% at 150 °C) occurred, CO conversion could be observed. Their major role for the reaction course is clearly indicated by the further boost in CO oxidation activity at higher temperatures and for larger amounts of $Pt_X^{\delta+}$. Considering the high reproducibility of the light-off/light-out cycles as well as the virtually same Pt-SS site

structure before and after the catalytic test, we assume that the *in situ* formed $Pt_X^{\delta+}$ clusters contain only few Pt atoms, which reoxidize and redisperse during cooling down in oxygen generating the initial Pt-SS state as described in the scheme in Fig. 6g-i.

CONCLUSIONS

Complementary surface and bulk characterization techniques, substantiated by DFT calculations allowed the detailed assignment of the Pt single site location on ceria after a typical high-temperature treatment. During single site formation at elevated temperatures planar square hollow positions, found e.g. at the {211} edge or generated by restructuring of the ceria surface lattice on the {110} facet or {221} edge, offer an ideal binding site for Pt^{2+} ions. UHV-FTIR results together with EXAFS analysis and DFT calculations indicate that such noble metal induced CeO_2-restructuring occurs above 600 °C. The *operando* HERFD-XAS and *in situ* UHV-FTIRS investigations furthermore confirmed that these Pt-SS are available for the adsorption and desorption of gas phase species even at low temperatures. Despite the interaction and high dispersion, Pt-SS performed poorly in CO, C_3H_6 or CH_4 oxidation compared to homogenously distributed Pt nanoparticles. DFT calculations suggest that such behaviour originates from the inhibition of the oxygen supply in a stable Pt^{2+}-CeO_2 structure that can adsorb CO, as Pt^{2+} reduction under the applied testing conditions is thermodynamically disadvantageous for the system. Therefore, higher temperatures are needed under lean conditions to initiate the generation of active $Pt_X^{\delta+}$ clusters. Such entities, most probably containing at least a few Pt atoms, seem to be essential for CO oxidation. This outcome is supported by a higher activity

of the same but pre-reduced catalyst, which becomes less active once the Pt sites are redispersed under lean reaction conditions. During reaction light-out, the *in situ* formed $Pt_X^{\delta+}$ clusters reoxidize and redisperse to the initial single site state. Consequently, the oxidation activity of Pt single sites is low, but highly reproducible compared to Pt nanoparticles. Hence, the stabilization of highly dispersed reduced clusters or higher dynamics of single sites on less interacting facets or different supports could be a promising approach to efficiently use the noble metal and maintain a high activity. In all cases, before concluding on the catalytic properties of single site catalysts and, in more general, to fully understand catalytic properties, tracking of the structure of the active species *in situ* upon interaction with the gas atmosphere and *operando* upon reaction onset is required. The use of additional complementary characterization tools, including theoretical DFT calculations, is essential for deriving and accurate conclusion on the catalytic performance of the active site.

EXPERIMENTAL SECTION

Catalyst preparation

Commercial ceria (MEL chemicals) was calcined at 700 °C for 5 h in order to reduce the amount of defect sites and triggering the formation of {111} facets (cf. Supplementary Table 5). A robot controlled incipient wetness impregnation (IWI) was performed using an Accelerator SLT106 Parallel Synthesizer – SLT CATIMPREG (ChemSpeed Technologies).[58] First, 1 g of ceria was placed in a batch reactor, then 0.16 mL of a 25.8x10-3 molar tetraammineplatinum(II) nitrate (99.995%, Sigmar-Aldrich) solution were added and dried under reduced pressure for 20 min at 70 °C. This step was repeated, until the desired platinum weight loading was achieved. The Pt/CeO_2 catalyst denoted as Pt-single site (Pt-SS), was first calcined at 500 °C for 5 h and then hydrothermally (10% O_2 and 10% H_2O in N_2) treated at 800 °C for 16 h. The catalyst was cooled down in steam until ~200 °C, then in 10 % O_2/N_2 to room temperature. For comparison, the same catalyst was reduced subsequently in 2% H_2 for 30 min at 400 °C to generate reduced Pt-nanoparticles (Pt-NP). For the catalytic tests and X-ray based characterization, Pt-NP was prepared *in situ* directly before the measurements.

Catalytic activity tests

The CO oxidation activity of Pt-SS and Pt-NP was evaluated using 50 mg of the granulated (125-250 µm) catalyst powder diluted with 450 mg of SiO_2 of the same sieve fraction in a plug flow reactor (ID: 8.0 mm, OD: 10.0 mm). The temperature in the reactor was monitored by two thermocouples up- and downstream of the catalyst bed. The upstream thermocouple was also used to control the furnace. For the Light Off (LO) tests, the catalyst was heated in an oxygen rich atmosphere (1000 ppm CO,

1000 ppm C_3H_6, 1000 ppm CH_4 or 1000 ppm CO and 150 ppm C_3H_6 and 8% O_2) from 50 °C to 500 °C with 10 K/min and hold at 500 °C for 1 h using a weight hourly space velocity (WHSV) of 60,000 L/g_{Pt}/h. These tests were repeated twice after each treatment. The gas concentration in the product flow was monitored on-line by a Fourier transformed infrared spectrometer (MultiGas™ 2030 FTIR Continuous Gas Analyzer, MKS Instruments).

Ex situ characterization

ICP-OES – The composition and platinum loading of the catalyst were determined by inductively coupled plasma optical emission spectrometry at the institute for applied materials of the KIT (Karlsruhe, Germany). The measurement was repeated two times. Prior to the analysis, the samples were digested using acids and high pressure.

BET – The pore volume and specific surface area were evaluated by N_2-physisorption using the Brunauer-Emmett-Teller method.[59] The samples were pretreated at 300 °C under reduced pressure (BELprep II, BEL Inc.). The N_2 physisorption itself was performed using a BELsorp II mini (BEL Inc.).

TEM – High angle annular dark-field imaging (HAADF) scanning transmission electron microscopy was performed at the laboratory for electron microscopy at the KIT (Karlsruhe, Germany) using a FEI Tecnai Osiris (Scanning) Transmission Electron Microscope at 80-300 kV. The particle size evaluation of Pt-NP was performed using ImageJ (version 1.52h). In total 557 particles were considered for the distribution.

XRD – Powder X-ray diffraction data were acquired in a 2Θ range of 20-100° with a step size of 0.0162° using a Bruker D8 advance XRD. The mean crystallite size of ceria for Pt-SS was determined by applying the Scherrer equation for the reflexes at 28°, 33° and 47° with a dimensionless shape factor of 0.94.

In situ characterization

A capillary micro reactor heated by a hot air gas blower (Oxford) was used as *in situ* cell.[60] Gases were dosed by mass flow controllers (Bronkhorst). The gas concentration in the product flow was monitored on-line by a mass spectrometer (Omnistar, Pfeiffer Vacuum) and a Fourier transformed infrared spectrometer (MultiGas™ 2030 FTIR Continuous Gas Analyzer, MKS Instruments). For the tests, the capillary reactor (1.5 mm outer diameter, 1.48 mm inner diameter) was loaded with 14 mg of the granulated (100-200 µm) Pt/CeO_2 catalyst sample.

Conventional X-ray absorption spectroscopy (XAS) in fluorescence mode was performed at the P65 beamline at the DESY (Hamburg, Germany). The incident energy (Pt L_3 edge) of the X-ray beam was pitched by a Si(111) crystal with an energy resolution of 1.4×10^{-4}. A 7 element Ge-detector was used to detect and select the emitted radiation of the sample. The beam size was 0.8 mm in vertical and 2.0 mm in horizontal. Scans were performed in step scanning mode. For transient measurements, X-ray absorption near edge spectra were collected from 11.413 to 11.905 keV, resulting in a time resolution of 11 min per scan or one spectrum every 55 K. For linear combination fitting, the as prepared Pt-SS was used as oxidized reference and the *in situ* reduced Pt-NP as reduced reference. Extended X-ray absorption fine structure spectra were recorded at room temperature in step scanning mode. The acquisition range was set to 11.314 to 13.056 keV. For the

EXAFS evaluation (details cf. Supplementary Table 2 and Supplementary Fig. 2), at least 2 spectra were merged to improve signal quality. Reference samples were measured as foil (Pt) or pellet (PtO_2).

High-Energy-Resolution Fluorescence Detected X-ray Absorption Near Edge Structure (HERFD XANES) measurements were recorded at the BM16/FAME-UHD beamline at the ESRF (Grenoble, France). A Si(220) double crystal monochromator was used to tune the incident energy (Pt L_3 edge) on the sample and three Ge(660) crystals were used to select the energy of the emitted fluorescence radiation ($L_{\alpha 1}$ emission line). The beam size on the sample was set to 150 x 300 µm. Spectra were recorded in step scanning mode with an energy resolution of 1-2 eV. *Operando* and *in situ* measurements were performed under steady state conditions. *Ex situ* measurements of reference powder samples were performed using capillaries to ensure the same geometry between incident beam, sample and detector. References for the linear combination analysis were extracted from *in situ* data recorded during TPR and TPO using the MCR-ALS method[54,55].

Ab initio calculations of XANES spectra

Pt L_3 edge XANES simulations were performed using the FDMNES[61] code (revision 01/2020). The self-consistent calculations were executed with the finite difference method, resulting in better agreement[62,63] with the experimental data than full multiple scattering approach and muffin tin approximation also implemented in FDMNES. Real Hedin–Lundqvist exchange–correlation potential and no core hole approximation were used. Parameters for *ab initio* XANES simulations were chosen based on the best agreement with experimental data (see Fig. 6 and Supplementary Fig. 29). For the comparison with experimental data, the calculated convoluted

spectra were shifted in energy by ΔE to align the energy scale used in theoretical calculations with the one of experimental spectra.

Density functional theory calculations

The density functional theory (DFT) calculations in this work are performed using the Vienna Ab Initio Simulation Package (VASP)[64,65] in connection with the Atomic Simulation Environment (ASE).[66] A plane-wave basis set with a cut-off energy of 450 eV, the projector augmented wave method (PAW)[67,68] and the Bayesian Error Estimation Functional with van der Waals correlations (BEEF-vdW)[69] exchange correlation functional were used. Due to the presence of delocalized Ce f orbitals, we applied GGA+U (U = 5.0 eV) method [70] in order to obtain more accurate energies. The infinite slab models, used to represent different facets of CeO_2, consist of a three {110} or four {111, 100, 211 and 221} layers thick 2x2x1 unit-cells, separated by more than 15 Å of vacuum in z direction. We tested the validity of the CeO_2 model using 5 CeO_2 layers in the z-direction and found no significant difference (cf. Supplementary Table 13 and Supplementary Fig. 30). Atoms in top two layers were allowed to relax during geometry optimizations. The Brillouin zones were sampled using (4x4x1) Monkhorst–Pack k-point grid[71] for {111} and {110} facets, (6x6x1) for {100} and (3x4x1) for {221} and {211} surfaces. The convergence criterion for geometry optimizations was a maximum force of 0.01 eV/Å. Spin polarization was considered in all calculations. Vibrational analyses were carried out in the harmonic approximation using finite difference with magnitude of displacements of 0.01 Å. Total DFT energies of reference materials are reported in Supplementary Table 7.

UHV-FTIR Spectroscopy and XPS

The ultra-high vacuum Fourier transformed infrared spectroscopy (UHV-FTIRS) and X-ray photoelectron spectroscopy (XPS) measurements were conducted with a sophisticated UHV apparatus combing a state-of-the-art FTIR spectrometer (Bruker Vertex 80v) and a multichamber UHV system (Prevac). This dedicated apparatus allows performing both IR transmission experiments on nanostructured powders and infrared reflection-absorption spectroscopy (IRRAS) measurements on well-defined model catalysts (single crystals and supported thin films). The Pt/CeO_2 powder sample (approximately 200 mg) was pressed into an inert metal mesh and then mounted on a sample holder specially designed for transmission FTIR measurements. Exposure to carbon monoxide (CO) was achieved using a leak-valve-based directional doser connected to a tube of 2 mm in diameter, which is terminated 3 cm from the sample surface and 50 cm from the hot-cathode ionization gauge. The IR experiments were carried out at temperatures as low as 113 K. The XPS experiments were performed using a VG Scienta R4000 electron energy analyser. The binding energies were calibrated using the C1s line at 284.8 eV as a reference. The XP spectra were deconvoluted using the software Casa XPS with a Gaussian-Lorentzian mix function and a Doniach−Sunjic function for metallic Pt^0 species.

DRIFTS

Diffuse reflectance infrared Fourier transform spectroscopy (DRIFTS) was performed using the VERTEX 70 FTIR spectrometer (Bruker) equipped with Praying Mantis diffuse reflection optics (Harrick) and a liquid nitrogen-cooled mercury cadmium telluride detector. The granulated catalyst (50 mg; sieve fraction: 125-

250 µm) was placed inside a high-temperature *in situ* cell (Harrick) covered by a CaF_2 window. The gas flow (300 mL/min) downwards through the sample compartment was analysed at the reactor exit with a ThermoStar quadrupole mass spectrometer (Pfeiffer Vacuum). After an oxidative treatment in 10% O_2 at 400 °C, the catalyst was cooled down to room temperature, flushed with inert gas (He) and exposed to 2% CO for 30 min. Subsequently the Pt-SS sample was kept 1 h under inert atmosphere (He) before spectra were collected.

Data Availability Statement

All data generated or analysed during this study are included in this published article (and its supplementary information files) or can be obtained from the authors upon reasonable request.

References

1. Deutschmann, O. & Grunwaldt, J.-D. Exhaust Gas Aftertreatment in Mobile Systems: Status, Challenges, and Perspectives. *Chemie Ing. Tech.* **85**, 595–617 (2013).
2. Liu, L. & Corma, A. Metal Catalysts for Heterogeneous Catalysis: From Single Atoms to Nanoclusters and Nanoparticles. *Chem. Rev.* **118**, 4981–5079 (2018).
3. Mitchell, S., Vorobyeva, E. & Pérez-Ramírez, J. The Multifaceted Reactivity of Single-Atom Heterogeneous Catalysts. *Angew. Chemie Int. Ed.* **57**, 15316–15329 (2018).
4. Beniya, A. & Higashi, S. Towards dense single-atom catalysts for future

automotive applications. *Nat. Catal.* **2**, 590–602 (2019).

5. Lin, J. *et al.* Remarkable Performance of Ir_1/FeO_X Single-Atom Catalyst in Water Gas Shift Reaction. *J. Am. Chem. Soc.* **135**, 15314–15317 (2013).
6. Neitzel, A. *et al.* Atomically Dispersed Pd, Ni, and Pt Species in Ceria-Based Catalysts: Principal Differences in Stability and Reactivity. *J. Phys. Chem. C* **120**, 9852–9862 (2016).
7. Therrien, A. J. *et al.* An atomic-scale view of single-site Pt catalysis for low-temperature CO oxidation. *Nat. Catal.* **1**, 192–198 (2018).
8. Chen, Z. *et al.* A heterogeneous single-atom palladium catalyst surpassing homogeneous systems for Suzuki coupling. *Nat. Nanotechnol.* **13**, 702–707 (2018).
9. DeRita, L. *et al.* Structural evolution of atomically dispersed Pt catalysts dictates reactivity. *Nat. Mater.* **18**, 746–751 (2019).
10. Tauster, S. J., Fung, S. C. & Garten, R. L. Strong metal-support interactions. Group 8 noble metals supported on titanium dioxide. *J. Am. Chem. Soc.* **100**, 170–175 (1978).
11. Haller, G. L. & Resasco, D. E. Metal–Support Interaction: Group VIII Metals and Reducible Oxides. *Adv. Catal.* **36**, 173–235 (1989).
12. Nagai, Y. *et al.* Sintering inhibition mechanism of platinum supported on ceria-based oxide and Pt-oxide–support interaction. *J. Catal.* **242**, 103–109 (2006).
13. Farmer, J. A. & Campbell, C. T. Ceria maintains smaller metal catalyst particles by strong metal-support bonding. *Science* **329**, 933–6 (2010).
14. Jones, J. *et al.* Thermally stable single-atom platinum-on-ceria catalysts via atom trapping. *Science* **353**, 150–4 (2016).
15. Daelman, N., Capdevila-Cortada, M. & López, N. Dynamic charge and

oxidation state of Pt/CeO_2 single-atom catalysts. *Nat. Mater.* **18**, 1215–1221 (2019).

16. Wang, X., Van Bokhoven, J. A. & Palagin, D. Atomically dispersed platinum on low index and stepped ceria surfaces: Phase diagrams and stability analysis. *Phys. Chem. Chem. Phys.* **22**, 28–38 (2019).
17. Dvořák, F. *et al.* Creating single-atom Pt-ceria catalysts by surface step decoration. *Nat. Commun.* **7**, 10801 (2016).
18. Kunwar, D. *et al.* Stabilizing High Metal Loadings of Thermally Stable Platinum Single Atoms on an Industrial Catalyst Support. *ACS Catal.* **9**, 3978–3990 (2019).
19. Feng, Y. *et al.* Correlating DFT Calculations with CO Oxidation Reactivity on Ga-Doped Pt/CeO_2 Single-Atom Catalysts. *J. Phys. Chem. C* **122**, 22460–22468 (2018).
20. Ke, J. *et al.* Strong Local Coordination Structure Effects on Subnanometer PtO_X Clusters over CeO_2 Nanowires Probed by Low-Temperature CO Oxidation. *ACS Catal.* **5**, 5164–5173 (2015).
21. Sayle, T. X. T., Parker, S. C. & Catlow, C. R. A. Surface Segregation of Metal Ions in Cerium Dioxide. *J. Phys. Chem.* **98**, 13625–13630 (1994).
22. Bruix, A. *et al.* Maximum Noble-Metal Efficiency in Catalytic Materials: Atomically Dispersed Surface Platinum. *Angew. Chemie Int. Ed.* **53**, 10525–10530 (2014).
23. Kottwitz, M. *et al.* Local Structure and Electronic State of Atomically Dispersed Pt Supported on Nanosized CeO_2. *ACS Catal.* **9**, 8738–8748 (2019).
24. Nie, L. *et al.* Activation of surface lattice oxygen in single-atom Pt/CeO_2 for low-temperature CO oxidation. *Science* **358**, 1419–1423 (2017).

25. Tang, Y., Wang, Y.-G. & Li, J. Theoretical Investigations of $Pt_1@CeO_2$ Single-Atom Catalyst for CO Oxidation. *J. Phys. Chem. C* **121**, 11281–11289 (2017).

26. Bera, P. *et al.* Promoting Effect of CeO_2 in Combustion Synthesized Pt/CeO_2 Catalyst for CO Oxidation. *J. Phys. Chem. B* **107**, 6122–6130 (2003).

27. Singh, P. & Hegde, M. S. Sonochemical Synthesis of Thermally Stable Hierarchical $Ce_{1-x}M_xO_{2-\delta}$ (M = Pt or Pd, $0 \leq x \leq 0.10$) Nanocrystallites: Redox Properties and Methanol Electro-Oxidation Activity. *Cryst. Growth Des.* **10**, 2995–3004 (2010).

28. Hegde, M. S. & Bera, P. Noble metal ion substituted CeO_2 catalysts: Electronic interaction between noble metal ions and CeO_2 lattice. *Catal. Today* **253**, 40–50 (2015).

29. Lee, J., Ryou, Y., Chan, X., Kim, T. J. & Kim, D. H. How Pt Interacts with CeO_2 under the Reducing and Oxidizing Environments at Elevated Temperature: The Origin of Improved Thermal Stability of Pt/CeO_2 Compared to CeO_2. *J. Phys. Chem. C* **120**, 25870–25879 (2016).

30. Cargnello, M. *et al.* Control of metal nanocrystal size reveals metal-support interface role for ceria catalysts. *Science* **341**, 771–3 (2013).

31. Bera, P. *et al.* Ionic dispersion of Pt over CeO_2 by the combustion method: Structural investigation by XRD, TEM, XPS, and EXAFS. *Chem. Mater.* **15**, 2049–2060 (2003).

32. Gatla, S. *et al.* Facile synthesis of high-surface area platinum-doped ceria for low temperature CO oxidation. *Catal. Today* **333**, 105–112 (2019).

33. Pereira-Hernández, X. I. *et al.* Tuning $Pt\text{-}CeO_2$ interactions by high-temperature vapor-phase synthesis for improved reducibility of lattice oxygen. *Nat. Commun.* **10**, 1358 (2019).

34. Wang, H. *et al.* Surpassing the single-atom catalytic activity limit through paired Pt-O-Pt ensemble built from isolated Pt1 atoms. *Nat. Commun.* **10**, 3808 (2019).

35. Gänzler, A. M. *et al.* Tuning the Structure of Platinum Particles on Ceria In Situ for Enhancing the Catalytic Performance of Exhaust Gas Catalysts. *Angew. Chemie Int. Ed.* **56**, 13078–13082 (2017).

36. Gorczyca, A. *et al.* Monitoring Morphology and Hydrogen Coverage of Nanometric Pt/γ-Al_2O_3 Particles by In Situ HERFD-XANES and Quantum Simulations. *Angew. Chemie Int. Ed.* **53**, 12426–12429 (2014).

37. Gänzler, A. M. *et al.* Operando spatially and time-resolved X-ray absorption spectroscopy and infrared thermography during oscillatory CO oxidation. *J. Catal.* **328**, 216–224 (2015).

38. Dessal, C. *et al.* Atmosphere-dependent stability and mobility of catalytic Pt single atoms and clusters on γ-Al_2O_3. *Nanoscale* **11**, 6897–6904 (2019).

39. Ye, X. *et al.* Insight of the stability and activity of platinum single atoms on ceria. *Nano Res.* **12**, 1401–1409 (2019).

40. Brogan, M. S., Dines, T. J. & Cairns, J. A. Raman spectroscopic study of the Pt–CeO_2 interaction in the Pt/Al_2O_3–CeO_2 catalyst. *J. Chem. Soc., Faraday Trans.* **90**, 1461–1466 (1994).

41. Branda, M. M., Ferullo, R. M., Causà, M. & Illas, F. Relative Stabilities of Low Index and Stepped CeO_2 Surfaces from Hybrid and GGA + U Implementations of Density Functional Theory. *J. Phys. Chem. C* **115**, 3716–3721 (2011).

42. Ding, K. *et al.* Identification of active sites in CO oxidation and water-gas shift over supported Pt catalysts. *Science* **350**, 189–92 (2015).

43. Chen, A. *et al.* Structure of the catalytically active copper–ceria interfacial

perimeter. *Nat. Catal.* **2**, 334–341 (2019).

44. Wang, Y. & Wöll, C. IR spectroscopic investigations of chemical and photochemical reactions on metal oxides: bridging the materials gap. *Chem. Soc. Rev.* **46**, 1875–1932 (2017).

45. Gänzler, A. M. *et al.* Tuning the Pt/CeO_2 Interface by in Situ Variation of the Pt Particle Size. *ACS Catal.* **8**, 4800–4811 (2018).

46. Safonova, O. V. *et al.* Identification of CO Adsorption Sites in Supported Pt Catalysts Using High-Energy-Resolution Fluorescence Detection X-ray Spectroscopy. *J. Phys. Chem. B* **110**, 16162–16164 (2006).

47. Singh, J. & van Bokhoven, J. A. Structure of alumina supported platinum catalysts of different particle size during CO oxidation using in situ IR and HERFD XAS. *Catal. Today* **155**, 199–205 (2010).

48. Lu, Y. *et al.* Identification of the active complex for CO oxidation over single-atom Ir-on-$MgAl_2O_4$ catalysts. *Nat. Catal.* **2**, 149–156 (2019).

49. Lang, R. *et al.* Non defect-stabilized thermally stable single-atom catalyst. *Nat. Commun.* **10**, 234 (2019).

50. Lott, P., Dolcet, P., Casapu, M., Grunwaldt, J.-D. & Deutschmann, O. The effect of pre-reduction on the performance of Pd/Al_2O_3 and Pd/CeO_2 catalysts during methane oxidation. *Ind. Eng. Chem. Res.* (2019).

51. Cullis, C. F. & Willatt, B. M. Oxidation of methane over supported precious metal catalysts. *J. Catal.* **83**, 267–285 (1983).

52. Casapu, M. *et al.* Origin of the Normal and Inverse Hysteresis Behavior during CO Oxidation over Pt/Al_2O_3. *ACS Catal.* **7**, 343–355 (2017).

53. Abedi, A., Hayes, R., Votsmeier, M. & Epling, W. S. Inverse Hysteresis Phenomena During CO and C_3H_6Oxidation over a Pt/Al_2O_3 Catalyst. *Catal.*

Letters **142**, 930–935 (2012).

54. de Juan, A., Jaumot, J. & Tauler, R. Multivariate Curve Resolution (MCR). Solving the mixture analysis problem. *Anal. Methods* **6**, 4964–4976 (2014).

55. Jaumot, J., de Juan, A. & Tauler, R. MCR-ALS GUI 2.0: New features and applications. *Chemom. Intell. Lab. Syst.* **140**, 1–12 (2015).

56. Voronov, A. *et al.* Multivariate curve resolution applied to in situ X-ray absorption spectroscopy data: An efficient tool for data processing and analysis. *Anal. Chim. Acta* **840**, 20–27 (2014).

57. Parkinson, G. S. *et al.* Carbon monoxide-induced adatom sintering in a Pd–Fe_3O_4 model catalyst. *Nat. Mater.* **12**, 724–728 (2013).

58. *Modern Applications of High Throughput R&D in Heterogeneous Catalysis*. (BENTHAM SCIENCE PUBLISHERS, 2014). doi:10.2174/97816080587231140101

59. Brunauer, S., Emmett, P. H. & Teller, E. Adsorption of Gases in Multimolecular Layers. *J. Am. Chem. Soc.* **60**, 309–319 (1938).

60. Grunwaldt, J.-D., Caravati, M., Hannemann, S. & Baiker, A. X-ray absorption spectroscopy under reaction conditions: suitability of different reaction cells for combined catalyst characterization and time-resolved studies. *Phys. Chem. Chem. Phys.* **6**, 3037 (2004).

61. Bunău, O. & Joly, Y. Self-consistent aspects of x-ray absorption calculations. *J. Phys. Condens. Matter* **21**, 345501 (2009).

62. Yan, H. *et al.* Atomic engineering of high-density isolated Co atoms on graphene with proximal-atom controlled reaction selectivity. *Nat. Commun.* **9**, 1–9 (2018).

63. Timoshenko, J., Lu, D., Lin, Y. & Frenkel, A. I. Supervised Machine-Learning-

Based Determination of Three-Dimensional Structure of Metallic Nanoparticles. *J. Phys. Chem. Lett.* **8**, 5091–5098 (2017).

64. Kresse, G. & Furthmüller, J. Efficient iterative schemes for *ab initio* total-energy calculations using a plane-wave basis set. *Phys. Rev. B* **54**, 11169–11186 (1996).

65. Kresse, G. & Furthmüller, J. Efficiency of ab-initio total energy calculations for metals and semiconductors using a plane-wave basis set. *Comput. Mater. Sci.* **6**, 15–50 (1996).

66. Bahn, S. R. & Jacobsen, K. W. An object-oriented scripting interface to a legacy electronic structure code. *Comput. Sci. Eng.* **4**, 56–66 (2002).

67. Blöchl, P. E. Projector augmented-wave method. *Phys. Rev. B* **50**, 17953–17979 (1994).

68. Kresse, G. & Joubert, D. From ultrasoft pseudopotentials to the projector augmented-wave method. *Phys. Rev. B* **59**, 1758–1775 (1999).

69. Wellendorff, J. *et al.* Density functionals for surface science: Exchange-correlation model development with Bayesian error estimation. *Phys. Rev. B* **85**, 235149 (2012).

70. Dudarev, S. L., Botton, G. A., Savrasov, S. Y., Humphreys, C. J. & Sutton, A. P. Electron-energy-loss spectra and the structural stability of nickel oxide: An LSDA+U study. *Phys. Rev. B* **57**, 1505–1509 (1998).

71. Monkhorst, H. J. & Pack, J. D. Special points for Brillouin-zone integrations. *Phys. Rev. B* **13**, 5188–5192 (1976).

Acknowledgements

F. Maurer (ITCP, KIT) gratefully thanks the “Fonds der Chemischen Industrie” (FCI) for financial support. J. Jelic and F. Studt acknowledge support by the state of Baden-Württemberg through bwHPC (bwunicluster and JUSTUS, RV bw16G001 and bwl17D011). J. Wang is grateful for a PhD fellowship donated by the China Scholarship Council (CSC). The authors further thank the German Federal Ministry for Economic Affairs and Energy (BMWi: 19U15014B) and the French National Research Agency (ANR-14-CE22-0011-02) for financial support of the ORCA project within the DEUFRAKO program, the DFG for financial support (INST 121384/16-1; INST 121384/73-1; INST 121384/73-1), DESY and ESRF for beamtime at the P65 and BM16 beamline, respectively. We thank D. Zengel, P. Lott, G. Cavusoglu and D. Doronkin (ITCP/IKFT, KIT) for assistance during *operando* XAS and HERFD-XANES experiments. Furthermore we acknowledge M. Stehle, A. Deutsch and J. Pesek (ITCP, KIT) for technical support with respect to catalyst preparation, characterization and testing as well as T. Bergfeldt (IAM-AWP, KIT) and H. Störmer (LEM, KIT) for ICP-OES analysis and HAADF-STEM, respectively. Finally, M. Rovezzi, A. Aguilar (BM16, ESRF), E. Welter, R. Nemausat and M. Herrmann (P65, DESY) are thanked for the support during beamtime at the corresponding beamlines. We also thank A. Zitolo (Samba, SOLEIL) for fruitful discussion on XANES data calculations.

Contributions

F.M. performed the catalyst preparation, X-ray based characterization, FEFF calculations, catalytic tests and wrote the paper. J.J. designed and performed the DFT calculations together with F.S. and wrote the corresponding text in the paper. J.W., Y.W and C.W. conducted the UHV-FTIRS and XPS characterization and interpretation. A.G. was involved in the DRIFTS and HERFD-XAS experiments as well as catalyst preparation. P.D. performed further catalytic tests, FDMNES calculations and helped in the FEFF calculations, in the analysis of the EXAFS and HERFD-XANES data. M.C. and J.-D.G. designed the study and co-wrote the paper. All the authors contributed to the interpretation of the results and commented on the manuscript.

Competing interests

The authors declare no competing interests.